Effects of Acoustic Actuation on a Multi-Phase Jet

Peter D Huck, Rodrigo Osuna-Orozco, Nathanaël Machicoane, Alberto Aliseda

Effects of Acoustic Actuation on a Multi-Phase Jet

Peter D. Huck*[1,2], Rodrigo Osuna-Orozco[1], Nathanael Machicoane[1,3], Alberto Aliseda[1,3]

[1]Mechanical Engineering Department, University of Washington, Seattle, USA
[2]Department of Mechanical and Aerospace Engineering, The George Washington University, Washington, DC, USA
[3]LEGI, Université Grenoble Alpes, Grenoble, France
*Corresponding author email: peterdhuck@gwu.edu

Abstract

In this contribution the effects of a nearly axisymmetric standing acoustic wave on the transport properties of a multi-phase jet are examined. The standing wave is seen to drive liquid droplets from the pressure anti-node , where the jet center-line is located towards the pressure node where the jet edge is located. Self-similarity of the gas-phase is modified in presence of the acoustics. Radial transport of the smallest particles is enhanced and saturation of this effect occurs as particle inertia increases. The overall volume flux profile of the jet is relatively unchanged but significant changes are observed in the number flux profile which is more sensitive to small particle dynamics. No evidence of enhanced atomization is observed, although the arithmetic mean diameter profiles are significantly altered due to modified transport.

Keywords

Turbulent transport, multi-phase jet, standing acoustic wave

Introduction

Acoustic instability is a naturally occurring phenomena in combustion chambers which can have deleterious effects on the fuel burning process. The interaction of a standing acoustic wave with a multi-phase turbulent jet is still an open question and offers the potential for closed loop control a burning fuel. A popular configuration for studying this problem is a square cylindrical chamber with high powered speakers oriented to produce the resonant 1T mode whereby a standing wave is produced with a wavelength equal to the dimensions of the cavity. Previously, authors have focused on the role of the location of the spray nozzle with respect to regions of maximal pressure, pressure anti-nodes (PAN), or minimal pressure, pressure nodes (PN) [1, 2, 3]. The so-called acoustic radiation force acts in the direction of negative rms pressure gradients imposing a force on the atomizing liquid. In general, liquid is driven from a PAN to a PN but atomization itself is promoted at the PN where a “squeezing” of the intact liquid core occurs which promotes destabilization and atomization [2]. Most effort in the interaction of an acoustic waves with sprays have focused on the atomization aspect of the spray. In this contribution we use Phase Doppler Interferometry to study the modification of particle transport in the spray when a co-axial atomizer is placed at the PAN of a forced standing wave. We find that transport from the PAN and PN is enhanced by the acoustic field, but only for the smallest particles. These observations are may inform closed loop control of sprays in unfavorable combustion scenarios.

Methods

The spray used herein results from a coaxial gas jet atomizing a central laminar liquid jet and is sketched schematically in figure 1(a). The central liquid jet forms a fully developed Poiseuille flow in the central channel and comes into contact with co-flowing air at the orifice which leads to

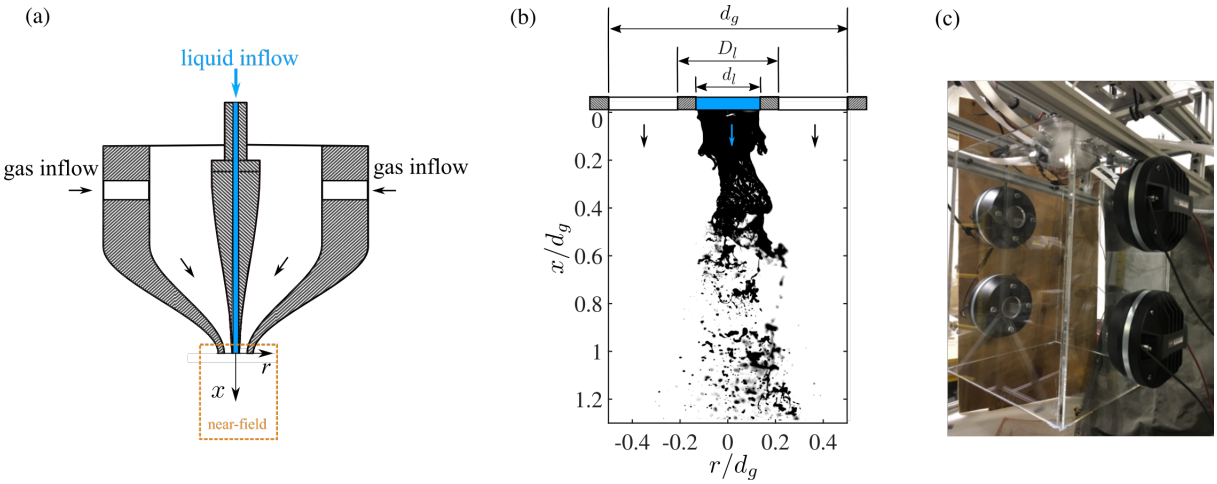

Figure 1. Experimental facility. (a) Co-axial atomizer used. (b) Example of spray produced in the experiments. (c) Acoustic chamber used in the experiments.

the development of the Kelvin-Helmholtz, and eventually Rayleigh-Taylor, instabilities followed by atomization of the liquid jet (figure 1 b). The diameter of the co-axial gas jet is d_g while the inner diameter d_ℓ and outer diameter D_ℓ characterize the central laminar liquid jet. The liquid velocity is given by $U_\ell = Q_\ell/A_\ell$ where $A_\ell = \pi d_\ell^2/4$ giving a liquid Reynolds number of $Re = U_\ell d_\ell/\nu_\ell$ where ν_ℓ is the kinematic viscosity at a laboratory temperature of 25°C. Four gas inlets are arranged perpendicular to the axis of the liquid flow resulting in a gas flow with zero momentum on average in the azimuthal direction. Four additional inlets are arranged off-axis to introduce additional gas flow with azimuthal momentum but are not used. The orthogonal gas inlets provide a volume flow rate of Q_g through an annular cross-section $A_g = \pi(d_g^2 - D_\ell^2)/4$ resulting in a gas velocity of $U_g = Q_g/A_g$ and a Reynolds number $Re_g = U_g d_g/\nu_g$. Additionally, the ratio of the dynamic pressure in the gas and liquid phases, known as the momentum ratio is given by $M = \rho_g U_g^2/(\rho_\ell U_\ell^2)$. The Weber number based on the average exit velocities is: $We = \rho_g(U_g - U_\ell)^2 d_\ell/\sigma$, where σ is the liquid-gas interface surface tension. The liquid mass loading which compares the liquid to gas flow rates is given by: $m = \rho_\ell A_\ell U_\ell/(\rho_g A_g U)$. The capillary number is: $Ca = u_\ell \eta_\ell/\sigma$. The same nozzle has been used previously [7] in a similar range of parameters as those presented here (table 1).

Phase Doppler Interferometry (PDI) and Laser Doppler Velocimetry (LDV) were used to gather point-wise, simultaneous measurements of radial and downstream velocities as well as particle diameters. The TSI LDV/PDI system (FSA4000 Signal Processor, PDM1000 Photo Detector Module) was operated in backward scattering with internal reflection the dominant mode at an observation angle of $\theta = 150°$. Standard intensity phase validation validation algorithms were followed to ensure quality particle size measurements.

An estimation of the probe volume viewed by the receiving probe was critical to properly determine the proper volume flux density in the experiments. An afocal relay system with a collimating lens ($f_c = 750\mu$m) and imaging lens ($f_i = 250\ \mu$m) was implemented to vary the magnification ($\beta = -f_i/f_c$). At the beam crossing the probe volume is approximately a prolate spheroid, however the use of a spatial slit filter ($s = 150\mu$m) truncates the volume along the major axis and permits a well defined probe length. Due to the collection angles employed the probe length was effectively longer than the slit by a factor of $1/\sin(\theta)$ and when accounting for the magnification employed the probe length could be calculated by $L = s/|\beta|\sin(\theta)$ [8]. The product of the particle longitudinal velocity and gate-time (*i.e.* residence time in the prove volume) gives a path length ℓ that is diameter dependent due to the gaussian nature of the laser

Re_g -	Re_ℓ -	M -	We -	m -	Ca $(\times 10^{-3})$	$P_{ac}(P_{rms})$ (Pa)	f_{ac} (Hz)
49200	1170	25.3	190.3	0.25	6.5	0(0)	-
49200	1170	25.3	190.3	0.25	6.5	2900(981)	1660
49200	1170	25.3	190.3	0.25	6.5	5300(1929)	1660
49200	1170	25.3	190.3	0.25	6.5	7100(2503)	1660

Table 1. Experimental parameters for an acoustically forced spray.

beam. In flows where the magnitude of the particle velocity is dominated by the longitudinal velocity such as particle laden round jets without swirl, particle trajectory effects in the probe volume are negligible and ℓ is essentially the diameter of the cylinder of length L. The diameter dependent probe area is then:

$$\mathcal{A} = \frac{\ell L}{|\beta| \sin\theta}. \tag{1}$$

and the probe volume is:

$$\mathcal{V} = \frac{\pi}{4} \frac{\ell^2 L}{|\beta| \sin\theta}. \tag{2}$$

A curve fit of ℓ as of function of d was performed to obtain the relevant probe area and volumes.

Acoustic actuation of the spray was achieved by placing the nozzle inside of an open ended chamber 43 cm long with square cross-sectional area 30.5cm on each side. The nozzle was placed 4cm from the top of the chamber oriented downwards. Four custom built B& C 1060 BST speakers were installed as shown in figure 1(c) such that the acoustic axis was perpendicular to the longitudinal axis of the spray. The resonant modes were modes were determined by solving the Helmholtz equations for this geometry. A forcing frequency of $f = 1660$ Hz was chosen to excite the first transverse mode of the chamber. The acoustic field was measured at several cross-sectional planes using a PCB 113B28 dynamic pressure sensor with sensing diameter of 5.54mm. The signal was amplified by a PCB 482C05 signal conditioner and the resulting analog signal was acquired with a NI-9239 acquisition card. The signal was acquired at 20 kHz to respect the Shannon criteria for the harmonics of the excited cavity.

Acoustic Field

Unlike experiments with a high aspect ratio acoustic chamber [1] where the wavelength be be a considered a standing wave with wavenlength $\lambda = 2\pi f/c$ where $c$is the speed of sound in air, the present chamber has an excited mode close to that of a closed rectangular cylinder:

$$f = \frac{c}{2}\sqrt{(\ell/L_x)^2 + (m/L_y)^2 + (n/L_z)^2)}, \tag{3}$$

where $L_x = L_y = 30.5\text{cm}$ and $L_z = 43.2$. The second transverse mode $(\ell, m, n) = (2, 2, 1)$ corresponds to a resonant frequence $f = 1639$ Hz, which is very close to the frequency determined by simulation $f = 1660$ Hz and at which these experiments where run. We note that the analogy of a closed rectangular cylinder is not exact in that the boundary conditions at the top and bottom of the chamber are different. To whit, the open cavity has pressure minima at either end while the closed cylinder enforces zero velocity boundary conditions which correspond to pressure maxima at either end. In either case, the nature of the resonant mode is the same, which allows us to estimate the fundamental frequency using equation 3.

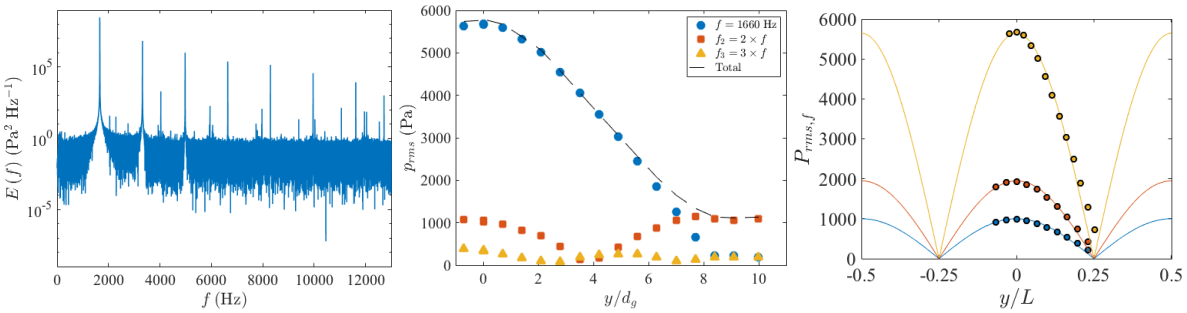

Figure 2. Acoustic measurements. (a) PSD of the acoustic signal at geometric center of chamber. (b) Total rms pressure of PSD plotted against the fundamental frequency and first two harmonics. (c) RMS pressure plotted at the geometric center of the chamber centered on the pressure anti-node.

The power spectrum density (PSD) of the pressure signal at the geometric center of the chamber is plotted in figure 4(a). The strength of the fundamental ($f = 1660$ Hz) is roughly 43 times stronger than the first harmonic ($f = 3320$) and 300 times stronger than the second harmonic ($f = 4980$ Hz) at the geometric center of the chamber. The rms of the pressure signal in the $y-$direction along the acoustic axis and perpendicular to the axis of the jet is plotted in figure 4(b). The pressure signal is maximum at $y/d_g = 0$, which is known as the pressure anti-node, and minimum at $y/d_g = 8$ known as the pressure anti-node. We see that the overtones contribute significantly near the pressure anti-node and prevent the total pressure rms from reaching $0Pa$. We note that [1] found that the values of the second harmonic to be one hundred times smaller than the fundamental in a facility with similar dimensions and found similar saturation at the velocity anti-node. However, it is attributed to the finite size of the pressure transducer in that work. We report the peak to peak pressures P_{ac} as well as rms pressures P_{rms} measured in this facility in table 1.

We isolate the contributions of the fundamental frequency to the spectrum by integrating a band of $f_0 \pm 200$ Hz which effectively isolates the strongest contributions of the signal. The fundamental is plotted in figures 4(c) for various forcing frequencies at the pressure anti-node and the pressure node (d). We note that the pressure node plot is in a direction perpendicular to the acoustic axis. We see that in oth cases the rms pressure approaches zero at $L/4$ as expected for a standing wave where L is the width of the chamber which corresponds to the wavelength of the fundamental mode. The acoustic field can be approximated by the (2,2,1) mode by:

$$p_{rms}(x, y, z) = p(0, 0, 0)|\cos(2\pi\ell x/L_x)\cos(2\pi m y/L_y)\cos(2\pi n z/L_z)|, \tag{4}$$

where the origin of the coordinate system is the geometric center of the chamber. This equation is plotted for several experimental conditions both at the pressure anti-node (figure 4b) and nodes (not shown) with satisfactory agreement.

Gas phase jet: unforced

In order to characterize the gas phase of the two-phase jet, the PDI data was conditioned for particle diameters roughly $d = 1\mu m$ in diameter. We calculate a Stokes number based on the exit conditions:

$$St_d = \frac{\tau_p}{d_g/U_g} \tag{5}$$

where $\tau_p = \rho_p d^2/(18\rho_g\nu)$ is the particle response time. We find that these particles have Stokes numbers in the range $St_d = 0.02$ for the range of Reynolds numbers considered here.

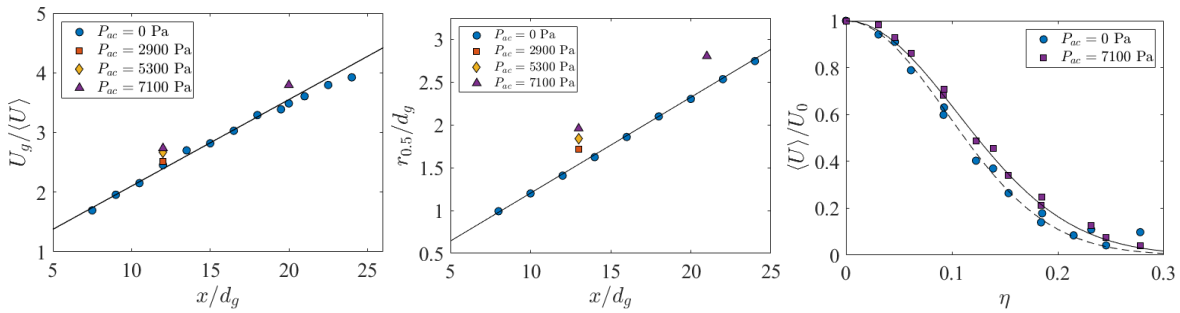

Figure 3. Gas phase evolution with and without acoustic forcing. (a) Reciprocal average velocity (solid symbols, $U_g/\langle U \rangle$) and reciprocal fluctuating velocity (open symbols, U_g/u') in the longitudinal direction. (b) Half-width of the longitudinal average velocity radial profiles (c) Self-similar longitudinal velocity profiles fit by equation 9 for $x/d_g = [13,\ 21]$. Dashed (solid) line is with (without) acoustic forcing.

The length (velocity) scale of the jet increases (decreases) with x leading to a time scale that increase as x^2. Therefore the Stokes number of these small particles decreases quickly with down stream position. We assume this particles to be adequate tracers of the flow. This claim is backed up *a posteriori* by comparisons presented below of the well known phenomenology of a self-similar turbulent round jet.

The evolution of the average centerline velocity with downstream location is plotted 3(a). Linear increase indicates that $\langle U \rangle \propto (x - x_0^{\langle U \rangle})^{-1}$. This evolution approximated by

$$\frac{U_g}{\langle U \rangle} = \frac{1}{B_{\langle U \rangle}} \frac{x - x_0^{\langle U \rangle}}{d_g}, \tag{6}$$

where $B_{\langle U \rangle}$ determines the average velocity decay rate and $x_0^{\langle U \rangle}$ is the relevant virtual origin which are given in table 1. Similar evolution of the average velocity was measured in the experiments of [9]. The evolution of the centerline fluctuating velocity is also plotted in figure 3(a) and is described by an equation analogous with equation 6 with constants $B_{u'}$ and $x_0^{u'}$ given in table 1.

As a consequence of the decay in the centerline velocity with x, the width of the jet is required to evolve as x to conserve momentum. The half-width ($r_{0.5}$) is defined as the position for which $\langle U \rangle = 0.5 U_0$ and is seen to evolve linearly in figure 3(c) as expected in a momentum-driven jet. We can calculate the spreading rate based on the half-width by:

$$r_{0.5} = S_{0.5}\left(x - x_0^{0.5}\right) \tag{7}$$

from which the spreading angle is calculated,

$$\theta_{0.5} = 2\tan^{-1}(S_{0.5}). \tag{8}$$

Both give agreement between the spreading rates found in the literature [9].

Evolution of the centerline mean velocity and radial spreading indicate self-similarity suggest self-similarity of the entire radial profile of longitudinal velocity. For a fully self-similar round jet the velocity profile should have a functional dependence on the radial coordinate $\eta = r/(x - x_0)$ such that $f(\eta) = \langle U(\eta) \rangle / U_0$. The functional dependence of the radial profile of the longitudinal velocity collapse onto a single curve in figure 3(d). A Gaussian functional dependence has been favored in the literature [9]:

$$\frac{\langle U \rangle}{U_0} = \exp(-C\eta^2). \tag{9}$$

$B_{\langle U \rangle}$	$x_0^{\langle U \rangle}$	$B_{u'}$	$x_0^{u'}$	$S_{0.5}$	$x_0^{0.5}$	$2\theta_{0.5}$	C
-	cm	-	cm	-	cm	deg	-
6.9	-4.5	1.3	-0.5	0.102	-0.75	12.8	55.0

Table 2. Table of constants calculated used to characterize the gas-phase longitudinal velocity profiles in a two-phase jet for $Re_g = 49200$. The decay rate of the average velocity (fluctuations) is given by $B_{\langle U \rangle}$ ($B_{u'}$) with the relevant virtual origins $x_0^{\langle U \rangle}$ ($x_0^{u'}$). The spreading rate of the half-width is given by $S_{0.5}$ with the virtual origin $x_0^{0.5}$. The opening angle defined by the half-width is $2\theta_{0.5}$. Longitudinal average velocity of the form in equation 9 is determined by C.

Figure 3(c) indicates that for the radial profiles of longitudinal velocity of approximately self-similar. These profiles are well approximated by equation 9 which is determined by C given in table 2. Similar values of C were found in [9].

Gas phase jet: forced

The average and fluctuating centerline velocity is modified by the presence of acoustics. In figure 3(a) as the acoustic forcing increases particle velocity on centerline decreases concomitantly at $x/d_g = [13,\ 21]$. Interestingly the decay coefficient $B_{\langle U \rangle}$ is preserved while increasing the forcing to its maximum value. The effect on the particle fluctuations is slight, though detectable. Modification of the gas phase by the acoustic field has been observed in LOx/H_2 experiments, increasing atomization due to an imposed velocity fluctuations [4]. In the present experiments, the acoustics appears to strongly affect the mean quantities.

While decay of the jet is enhanced, its self-similar nature is preserved. Similarly, the radial expansion of the jet as measured by $r_{0.5}$ is enhanced by presence of acoustics in figure 3(b). Increased radial expansion is coherent with the augmented longitudinal decay of the centerline velocity. Although we have only two measurement points at $P_{ac} = 7100$ Pa it appears that the expansion coefficient $S_{0.5}$ is also preserved for high acoustic forcing, in agreement with observations for the longitudinal decay.

The overall modification of the velocity profile inferred from the average and fluctuating velocities as well as the spreading rate implies preserved self-similarity of the gas phase in the presence of acoustic forcing. The self-similar gas phase profiles are plotted only for the zero and maximal forcing cases for clarity. Collapse of the profiles at $x/d_g = [13,\ 21]$ is evident which is in agreement with the preservation of self-similarity observed in the average velocity and spreading rates. However, the form of the profiles is modified due to the acoustics. These profiles could be made to collapse with a suitable choice of the virtual origin for the acoustics case: $x_0^{\langle U \rangle}/d_g = -6.5$.

Acoustic actuation on the spray

The acoustic field has a direct effect on the spatial organization of the particles in the far-field of the jet. In figure 4a the radial profile of the arithmetic average (d_{10}) droplet size is plotted as a function of acoustic forcing. On the centerline there is an increase in d_{10} while the value on the edges decreases. Interestingly, the overall value of d_{10} for the spray is unchanged (not shown,$d_{10} = 17\ \mu$m) which implies that the evolution of the radial profiles is not due to modified fragmentation but to modified transport due to the acoustic forcing.

The number flux density (NFD) is defined as the number of particles for given size class that

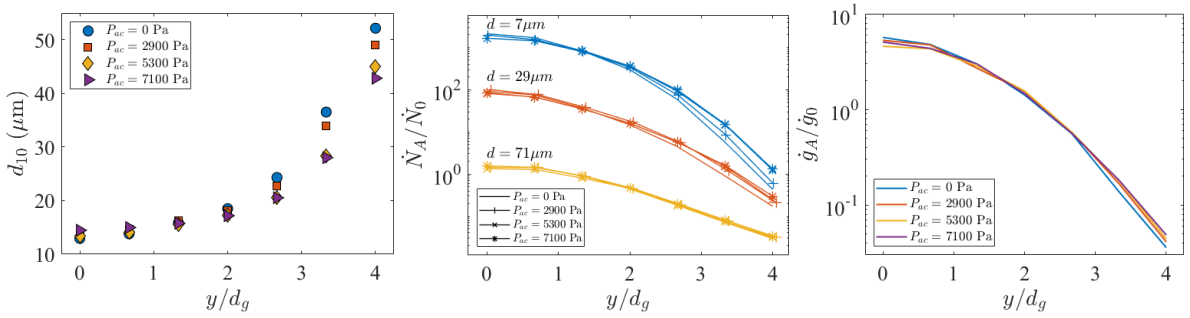

Figure 4. Radial transport of particles as a function of acoustic forcing. (a) Arithmetic mean (d_{10}). (b) Number flux density for $d = [7, 29, 71]$ μm correspond to blue, red, yellow curves respectively. c) Total volume flux density.

pass through a unit area. We calculate the NFD for the i^{th} size class as:

$$\dot{n}(d_i) = \frac{\pi}{6T_s} \sum_{j=1}^{N_i} \frac{1}{\mathcal{A}_{j,i}}, \tag{10}$$

where T_s is the total sample time, $\mathcal{A}_{j,i}$ is the probe cross section calculated in equation 1 of the j^{th} particle of the i^{th} size class with diameter d_i. Similarly the volumme flux density is calculated by:

$$\dot{g}(d_i) = \frac{\pi}{6T_s} \sum_{j=1}^{N_i} \frac{d_{j,i}^3}{\mathcal{A}_{j,i}}. \tag{11}$$

By integrating over all D size classes we obtain the total number flux density:

$$\dot{N} = \sum_{i=1}^{D} \dot{n}(d_i), \tag{12}$$

as well as the total volume flux density

$$\dot{G} = \sum_{i=1}^{D} \dot{g}(d_i), \tag{13}$$

The number flux density per size class (equation 10 is plotted in figure 4(b) for $d = [7, 29, 71]$ μm as a function of the acoustic forcing. For the smallest size class ($d = 7$ μm) there is a growing deficit on the centerline as the acoustic forcing increases and a concomitant increase on the edges. For the next size class ($d = 29$ μm) the tendency is the same, albeit with a smaller relative difference between the different acoustic forcings. The largest size class ($d = 71$ μm) displays no variation with acoustic forcing. There apperas to be a decreasing affect of the acoustic field on particle transport. Monotonic decrease in the particle response to a standing wave has been derived theoretically [5, 6]. Increased radial transport helps to explain the small increase of d_{10} on the centerline where small particles are removed preferentially. These particles then populate the edges, lowering the d_{10} there. However, if we look at the total volume flux density (eq. 13) in figure 4(c) there is a measureable, but weak, change in the profiles as the acoustic forcing is increased. The smallest particles experience enhanced radial transport with respect to the large ones and contribute far less to the volume flux density on a particle by particle basis.

Acoustic forcing has a strong effect on the local number flux, however, the over all volume

flux density (eq. 13) is much less sensitive to acoustic forcing. In figure 4(c), the total volume flux density is plotted as a function of the acoustic forcing. Although there appears to be a small decrease in flux on the centerline and increase on the edges, it is smaller than that measured by the number flux. The enhanced transport of the smallest particles is most visible in the number flux. However, the volume flux, which is proportional to d^3 (eq. 10), is weighted to the dynamics of the largest particles which are more insensitive to acoustic forcing.

Conclusion

In this contribution a high momentum ratio spray was investigated in the presence of an standing acoustic wave of varying intensity. The longitudinal velocity of small particles was measured to probe the gas phase of spray. Typical self-similar quantities such as the longitudinal velocity on the centerline, spreading rate, and self similar velocity profiles were measured to be in agreement with the literature. In the presence of forcing these the acoustic forcing these profiles were modified, but the self-similar nature was retained. Evidence for enhanced radial transport of the smallest particles was presented. The presence of an acoustic field drives small particles from the center of the jet to the edge, modifying the local arithmetic mean diameter as well as the number flux. Small paritcles appear to be more susceptible to enhanced transport than large ones, in agreement with theoretical predictions. The volume flux is mostly unchanged by acoustic forcing due to its relative insensitivity to the dynamics of small particles. The results presented herein may provide insight into control strategies using acoustic fields in the context of liquid combustion.

Acknowledgements

This work was sponsored by the Office of Naval Research (ONR), as part of the Multidisciplinary University Research Initiatives (MURI) Program, under grant number N00014-16-1-2617.

References

[1] Baillot, F., Blaisot, J., Boisdron, G., Dumouchel, C., 2009, *Journal of Fluid Mechanics*, 640, pp. 305-342.
[2] Ficuciello, A., Blaisot, J., Richard, C., Baillot, F., *Physics of Fluids*, 29 (6).
[3] Carpentier, J-B., Baillot, F., Blaisot, J., Dumouchel, C., 2009, *Physics of Fluids*, 21 (2).
[4] Hardi, J., Martinez, H., Oschwald, M., Dally, B., 2-14, *Journal of Propulsion and Power*, 30 (2), pp. 337-349.
[5] Annamalai, S., Balachandar, S., Parmar, M., 2014, *Physical Review E*, 89 (5), pp. 1-13.
[6] Annamalai, S. , Balachandar, S., 2015, *Physics of Fluids*, 27 (10).
[7] Machicoane, N. , Bothell, J. , Li, D. , Morgan, T., Heindel, T., Kastengren, A. , Aliseda, A., 2019, *International Journal of Multiphase Flow*, 115, pp. 1-8.
[8] Albrecht, H.E. , Borys, M. Damaschke, E., Tropea, C., 2003, “Laser doppler and phase doppler measurement techniques”. Springer Berlin Heidelberg.
[9] Panchapakesan, N.R., Lumley, J., 1993, *Journal of Fluid Mechanics*, 246, pp. 197-223.